



Effects of static and dynamic femtosecond laser modifications of Ti/Zr multilayer thin films

Suzana Petrović^{1,a}, G. D. Tsibidis², A. Kovačević³, N. Božinović¹, D. Peruško¹, A. Mimidis², A. Manousaki², and E. Stratakis²

¹ Department of Atomic Physics, “VINČA” Institute of Nuclear Sciences - National Institute of the Republic of Serbia, University of Belgrade, P.O.Box 522, Belgrade 11001, Serbia

² Institute of Electronic Structure and Laser (IESL), Foundation for Research and Technology (FORTH), N. Plastira 100, Vassilika Vouton, 70013 Heraklion, Crete, Greece

³ Institute of Physics, University of Belgrade, Pregrevica 118, Belgrade 11080, Serbia

Received 30 March 2021 / Accepted 13 October 2021 / Published online 7 December 2021
© The Author(s) 2021

Abstract. The experimental study of the static and dynamic femtosecond laser ablation of the multilayer 15x(Ti/Zr)/Si system is reported. The layer-by-layer selective laser ablation mechanism was studied by analysis of the surface morphology and elemental composition in static single pulse irradiation in a range of pulse energy from 10 to 17 μJ . The selective ablations, as number of concentric circles in modified spots are increased with the pulse energy. The boundary between the circles was shown a change in the depth, comparable to the thickness of the individual layers. Changes in the elemental composition at the edges are associated with the removal of the layer by layer. The dynamic multipulse irradiation was observed via the production of lines with laser-induced periodic surface structures (LIPSS) at different laser parameters (scan velocities and laser polarization). The spatial periodicity of the formed LIPSS depends on changes in the effective number of pulses and laser polarization, as well as the nature of the material. For better interpretation of the experimental results, simulations have been conducted to explore the thermal response of the multiple layered structure 15x(Ti/Zr) after static single pulse irradiation.

1 Introduction

Micron and nano-scaled surface structuring confer additional functionalities to the material in terms of mechanical improving, bioactivation and photonic selectivity. Ultrafast laser surface modification has become a powerful tool in high quality surface texturing of a wide range of materials including metals, ceramics, semi-conductors and plastics [1–4]. The material processing such as ultrafast laser-surface structuring can enable specific features of the materials including extraordinary surface wettability, reduction of friction and wear, improve corrosion resistance, colorization of metallic surface, and also improve solar cell performance and activation of biomaterials [5–8]. Simply by irradiating different materials with ultrashort laser pulses in the various ambient conditions, the following surface structures can be formed: ripples, grooves, spikes, bumps, cavities, nanoparticles and cellular structures. The creation of these structures during the laser processing is caused by thermal and non-thermal processes such as plasma formation, interference effects, Coulomb’s explosion, surface plasmon generation, surface tension gradients, as well as hydrodynamical effects [9–11].

Laser ablation of solids is a complex process of removing materials in combination by evaporation, melting, explosion and exfoliation of materials, while the interaction mechanism is determined by the nature of the material and applied laser parameters. Laser pulse duration plays a critical role in the ablation of materials. The ablation process induced by nanosecond laser pulses generates huge heat-affected zones (HAZ) with a wide molten area of metallic materials due to their large thermal diffusivities [12]. However, femtosecond laser ablation results in precise modification without collateral damages, due to suppress heat diffusion to the surroundings of irradiated regions, which significantly reduces the generation of a heat-affected zone (HAZ). In femtosecond time domain the excitation of multiphoton and avalanche ionization together with free electron heating are occurred, but without significant changing the lattice temperature [13–15].

In addition, after multiple-pulse laser ablation it is possible to generate laser-induced periodic surface structures (LIPSS) on numerous types of materials attractive for many applications. Irradiation of metallic surfaces by linearly polarised ultrashort laser pulses can induce shallow periodic corrugations with sub-wavelength spatial periods [16,17]. When the spatial periodicity of LIPSS is almost equal to the laser wave-

^a e-mail: spetro@vin.bg.ac.rs (corresponding author)

length, they are classified as low spatial frequency LIPSS (LSFL). The creation of LSFL is explained by the interference between the incidence laser beam and the surface-scattered electromagnetic wave, which induces a periodic variation of laser intensity along the surface. On the other hand, high spatial frequency LIPSS (HSFL) has much smaller spatial periodicity. Several interpretations have been proposed for their creation, such as self-organization, second harmonic generation, excitation of surface plasmon polaritons, and Coulomb explosion [18–20]. Lately, the progress in the field of ultrafast laser processing based on ablation is very important, including surface micro- and nano-patterning as well as 2D-surface and 3D-volume processing.

An unusual form of the material, like nano-scaled metallic multilayer thin films, attracts attention to specific applications in areas where superficial materials are decisive factor. Mostly, metallic thin films possess specific physico-chemical and mechanical properties as high corrosion resistance, good radiation stability, satisfactory hardness and porosity. Multilayer thin films are suitable material for a wide range of application, as protective coatings, catalytic components, optical devices, photovoltaic gas sensors, dye sensitized solar cells, in biomedicine as implants and tools [21–23]. Multilayer thin film is inherently metastable state and susceptible to various surface modifications, especially laser processing on the micro- and nanoscale by direct patterning in a very fast and cost-effective manner [24].

In this work, we study the possibility to achieving the selective ablation as well as the formation of LIPSS on the multilayer Ti/Zr thin films [25]. Layer-by-layer selective ablation would be predicted from experimental results obtained after a static single fs pulse irradiation. The depth and elemental composition of the ablated circular spots are comparable to the thicknesses of individual layers as a part of the multilayer structure. The ablation study of the multilayer systems is included a detail analysis of the influence of scan speed and laser beam polarization on the spatial periodicity of the formed LIPSS in ablative regime during the dynamic fs irradiation.

2 Experimental

The multilayer structures composed of titanium and zirconium layers were deposited in a Balzers Sputtrion II system, using 1.3 keV argon ions and 99.9% pure Ti and Zr targets. Before deposition the chamber was evacuated to the base pressure of 1×10^{-6} mbar, while the Ar partial pressure during deposition was 1×10^{-3} mbar. For substrate has selected a silicon wafer Si (100), which was cleaned by etching in HF and immersion in deionized water before mounting in the chamber. The deposition of multilayers was performed in a single vacuum run, at deposition rate of 0.17 nm s^{-1} for both Ti and Zr components, without heating of the substrates. The total thickness of the complete multilayer structure

consisted of fifteen (Ti/Zr) bilayers was 500 nm, where thickness of individual Ti and Zr layers were about 17 nm.

Laser processing of the multilayer 15x(Ti/Zr) thin films was performed by two laser systems. One is the Yb:KGW laser source Pharos SP from Light Conversion. The surface of thin films was irradiated by focused linearly p-polarised pulses with follow characteristics: repetition rate of 1 kHz, pulse duration equal to 160 fs, central wavelength of 1030 nm and $40 \mu\text{m}$ Gaussian beam diameter. The other is Ti:S laser system Mira 900 by Coherent, a source of linearly polarised ~ 130 fs pulses with 76 MHz repetition, wavelength of 860 nm and 600 nm Gaussian beam diameter. Mounted on a motorized, computer-controlled X-Y-Z translation stage, samples were processed by laser beam at normal incidence in open air environment. By irradiation of Ti/Zr samples with different pulse energy/fluence and scan velocities, i.e. number of pulses, respectively, formation of spots and lines were included. In each line, energy per pulse was assumed to be constant, since the pulse energy deviation was less than 1%.

Detailed surface morphology after irradiation was examined firstly by optical microscopy, and then by scanning electron microscopy (JEOL JSM-7500F, equipped with energy dispersive X-ray spectroscopy—EDS—by Oxford Instruments INCA, and Tescan MIRA3 SEM). The laser-modified and ablated surface profiles were studied in 2D- and 3D-modes using an optical profiler 7300 SWLI (Zygo).

3 Results and discussion

The effects of morphological changes induced during the static single fs pulse irradiation performed on the 15x(Ti/Zr)/Si system were examined through the spots made at the different pulse energies (Fig 1). For all applied pulse energies, a circular ablated spot with a distinct sharp boundary between unmodified and ablated areas occurred. The lowest absorbed pulse energy ($10 \mu\text{J}$) exceeds the kinetic energy of the removed material, whereby the ablation occurs in the form of a very shallow and flat crater (Fig. 1a). With an increase in the pulse energy, the number of concentric circles in observed individual spots increased (Fig. 1b–d), which can be attributed to the selective ablation of the multilayer 15x(Ti/Zr) /Si system. However, the number of circles (four) is same for pulse energies of $15 \mu\text{J}$ and $17 \mu\text{J}$, and with further increasing of pulse energy the number of circles remains constant, whereby for sufficiently high pulse energies the circles disappear. For the given range of pulse energies, the spot diameters had values from 27 to $47 \mu\text{m}$. According to the established procedure, the ablation threshold fluence F_{th} can be experimentally determined by representing squared diameter of the ablated areas D^2 as a function of the logarithm of the applied pulse energies E_p , for the fs laser pulse and Gaussian distribution [26,27]. The cal-

culated ablation threshold fluence for the multilayer 15x(Ti/Zr)/Si system is $F_{th} = (220 \pm 40) \text{ mJ cm}^{-2}$.

Simultaneously, the selective ablation of multilayer system can be recognized in the corresponding depth profiles displayed with SEM images (Fig. 1). Maximum depth in the centre of spots is gradually rising with pulse energy. The height/depth of the removed material almost match with the thickness of as-deposited layers (thicknesses of individual layer were 17 nm), these insignificant deviations can be attributed to measurement errors ($\sim 5\%$ deviations in the profilometric measurement). The differences in dimension (height and width) of the ablated steps originated from a different distribution of energy in Gaussian profile for given pulse energy. The boundaries between the ablated steps closer to the central part of the spot indicate a partial melting of Ti and/or Zr layers (Fig. 1c, d), also can be consequence of Gaussian energy distribution. The arrangement of concentric circles corresponding to selective ablation can be related to Gaussian spatial beam fluence profile, which is schematically presented in (Fig. 2.) [28]. The fluence of each ablated area was estimated from Gaussian profile (Fig. 2) and calculated by $F = F_0 \exp(-2r^2/\omega_0^2)$ equation for surface modification obtained at a pulse energy of $17 \mu\text{J}$ and the fluence at the centre of 597 mJ cm^{-2} [28]. The estimated values of ablated steps from periphery to the centre are $F_1 = 342 \text{ mJ cm}^{-2}$, $F_2 = 418 \text{ mJ cm}^{-2}$ and $F_3 = 503 \text{ mJ cm}^{-2}$.

The EDS analysis of the 15x(Ti/Zr) /Si multilayer system was performed in order to compare the differences in the elemental composition of unmodified multilayer thin film and the ablated steps for the spot made at the average pulse energy of $17 \mu\text{J}$. The EDS spectra recorded at particular points in the different steps are given in Fig. 3. Obviously, the ablation effects observed from periphery to the centre of the spot are confirmed by gradually increasing of the relative concentration of silicon [in spectrum 2, peak for Si (Fig. 3)], is attributed to the contribution of the substrate in regard to unmodified area of the 15x(Ti/Zr) /Si multilayer system. However, the relative concentrations of Ti and Zr change quite differently, in the ablated steps where the concentration of Ti decreases, the concentration Zr remains unchanged and vice versa. The concentration of Ti decreases in first and third steps, while in the second step is recorded the reduction of the Zr concentration. These distribution of the Ti and Zr contents through the ablated steps indicate that the layer-by-layer selective ablation are occurred during the static single fs irradiation of multilayer 15x(Ti/Zr) /Si thin film.

In the fourth central step, the concentrations of Ti and Zr simultaneously decrease, indicating the peak fluence is high enough to cause the mixing of components between the layers. Additionally, with decreasing concentrations of the main components (Ti and Zr) from periphery to centre of spot, the quantity of bonded oxygen is increased, which is also associated with Gaussian energy distribution for given pulse energy. Due to the intermixing of components and higher content of oxy-

gen in the central area of ablated spots, it is expected that an ultra-thin layer composed of Ti and Zr oxide phases is formed at the bottom of the ablated centre [29].

Effects of the dynamic fs modification of multilayer 15x(Ti/Zr) /Si system is considered during the formation of lines with different scan velocities at the constant pulse energy ($2.5 \mu\text{J}$) and with laser beam polarisation parallel to scan direction. For the selected scan velocities range ($0.5\text{--}3 \text{ mm s}^{-1}$), in all cases, the creation of the laser-induced periodic surface structures (LIPSS), oriented normally to the direction of laser polarization have occurred (Fig. 4). In the midline, the well-defined LIPSS (LSFL) are created, originating from an interference of the incident laser beam with surface electromagnetic wave excited during the laser irradiation [30]. Created ripples are oriented parallel to the scan direction and their length almost coincides with the width of the lines for lower scan velocities. The formation of ripple surface structures is followed with the significant ablation of multilayer 15x(Ti/Zr) /Si as well as hydrodynamical effects system, but ripples are somewhere covered with nanoparticles with dimensions of up to 100 nm. The ripples mainly are formed on the surface of Ti/Zr thin film although the ablation of materials is significant, at the highest scan velocity with the effective number of pulses was $N_{\text{eff}} = 266$ (Fig. 4a). The concentration for Ti and Zr components recorded by EDX method, are reduced (for 40 % wt.) in compare to the unmodified surface of the multilayer 15x(Ti/Zr) /Si thin film. With a reduction of the scan velocity, the ablation of the material is enhanced, whereby the Ti/Zr thin film for the lowest velocity and the highest effective number of pulses (0.5 mms^{-1} and $N_{\text{eff}} = 1600$) is completely removed and the ripples are formed on a silicon substrate (Fig. 4d). Furthermore, in the midline, made with the highest pulse number, a starting stage of the regularity failure of the ripple structure and/or formation of the grooves can be recognized as appearance of clusters on the surface of silicon. In this case, the EDS analysis was shown that the concentrations of Ti and Zr components dropped to zero, while the concentration of Si increased with the presence of oxygen in a relatively low concentration (about 5% wt.).

The fs modification in the form of lines, obtained with another laser polarisation (changed for 90°) and with all laser parameters same as in the previous case, has shown a very similar morphological characteristics and composition changes (Fig. 5). The ripples as LSFL are oriented along the scan direction, but perpendicular to the laser polarization. For higher number of applied pulses, the ablation becomes more intense, e.g. with an effective 1600 pulses for a scan velocity of 0.5 mm s^{-1} , the thin film is completely ablated and the ripple structure is formed on silicon. For the given laser polarisation, the modulation of ripples can be recognized in the sense that their length changes for the different scan velocities. This modulation can be associated with the number of overlapped pulses for various scan velocities, which would mean that the ripple lengths would be shortened with the scan velocities due to the

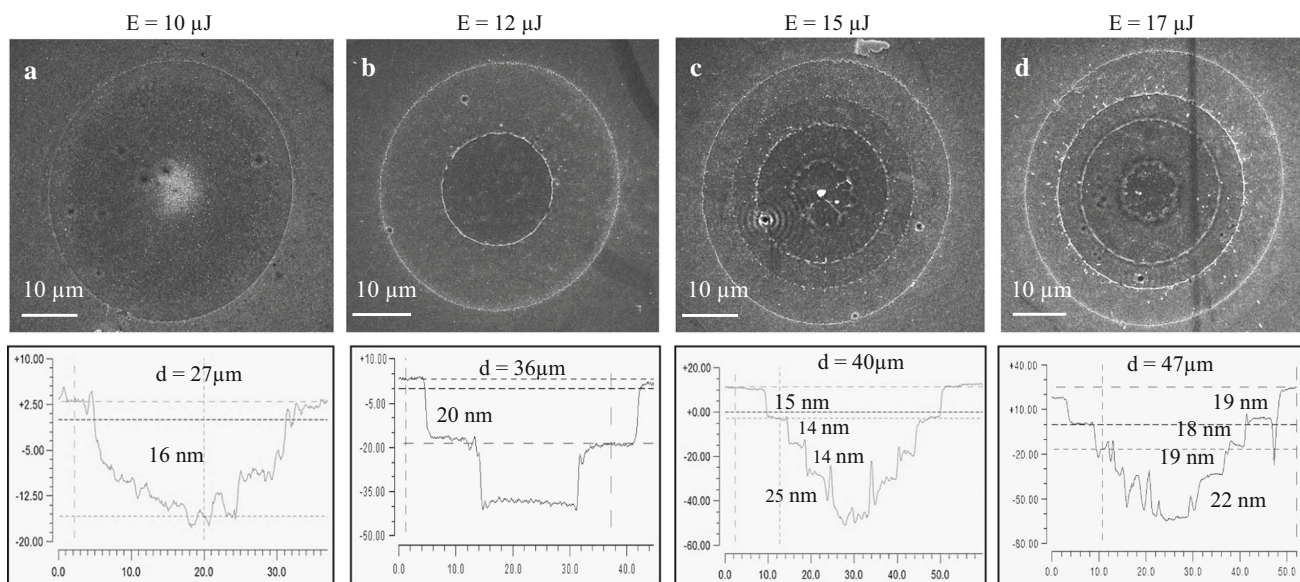


Fig. 1 SEM images and corresponding profiles at the surface of 15x(Ti/Zr)/Si multilayer system for spots made by femtosecond laser pulses at different pulse energies in follow range **a** 10 μJ, **b** 12 μJ, **c** 15 μJ and **d** 17 μJ

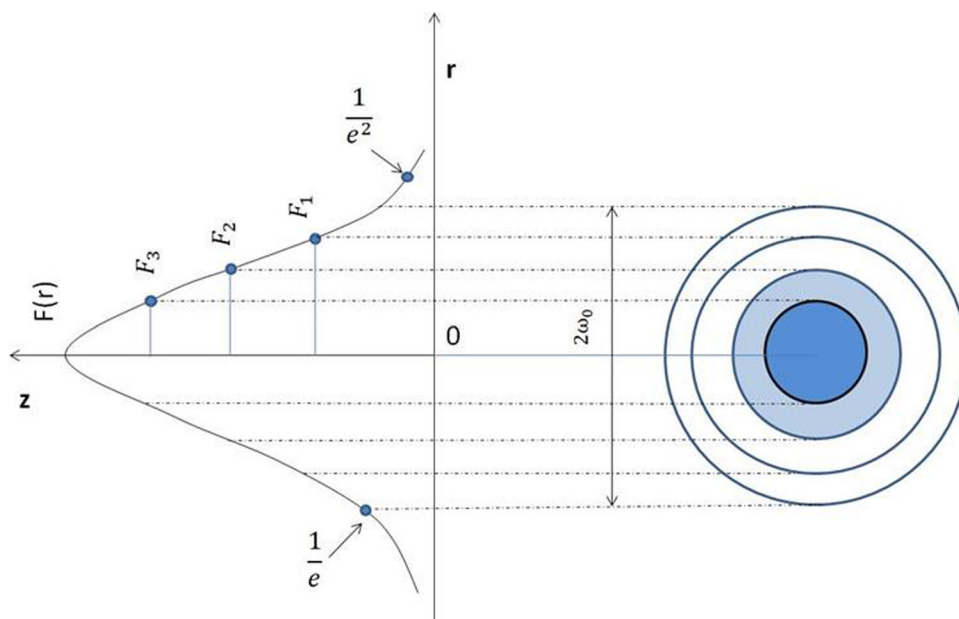


Fig. 2 Illustration of Gaussian fluence profile for laser ablation at pulse energy of 17 μJ

increase of the overlapping factor. The ripple lengths are in the range of 4–9 μm, where one number of ripples is ended or other can be continued from bifurcation points. These values of ripple length coincide with the mean free path of excited surface plasmon polaritons (SPP) for Ti irradiated with laser pulses at wavelength of 1030 nm [30]. It has been found that titanium has small SPP mean free path, which supports good coherence between excited SPP and incident laser radiation, favouring the formation of high regularity LIPSS [31].

The lines drawn by laser beam at different scan velocities, which is actually dynamic multipulse irradiation with different effective number of pulses, induce the

creation of the laser-induced periodic surface structures (LIPSS) with different spatial periodicity. The spatial periodicities of the created LSFL at the given range of effective number of pulses have shown tendency to reduction with their increasing, for both used laser polarizations (Fig. 6). The reduction in the spatial period is observed up to 800 pulses, afterwards for the highest applied pulses (1600), in fact at the smallest scan velocity (0.5 mm s⁻¹), the spatial period in both cases is increased. The sudden increase of the spatial periods can be associated with the fact that the ripple structures for a given scanning speed of 0.5 mm s⁻¹ were created on a silicon substrate due to inten-

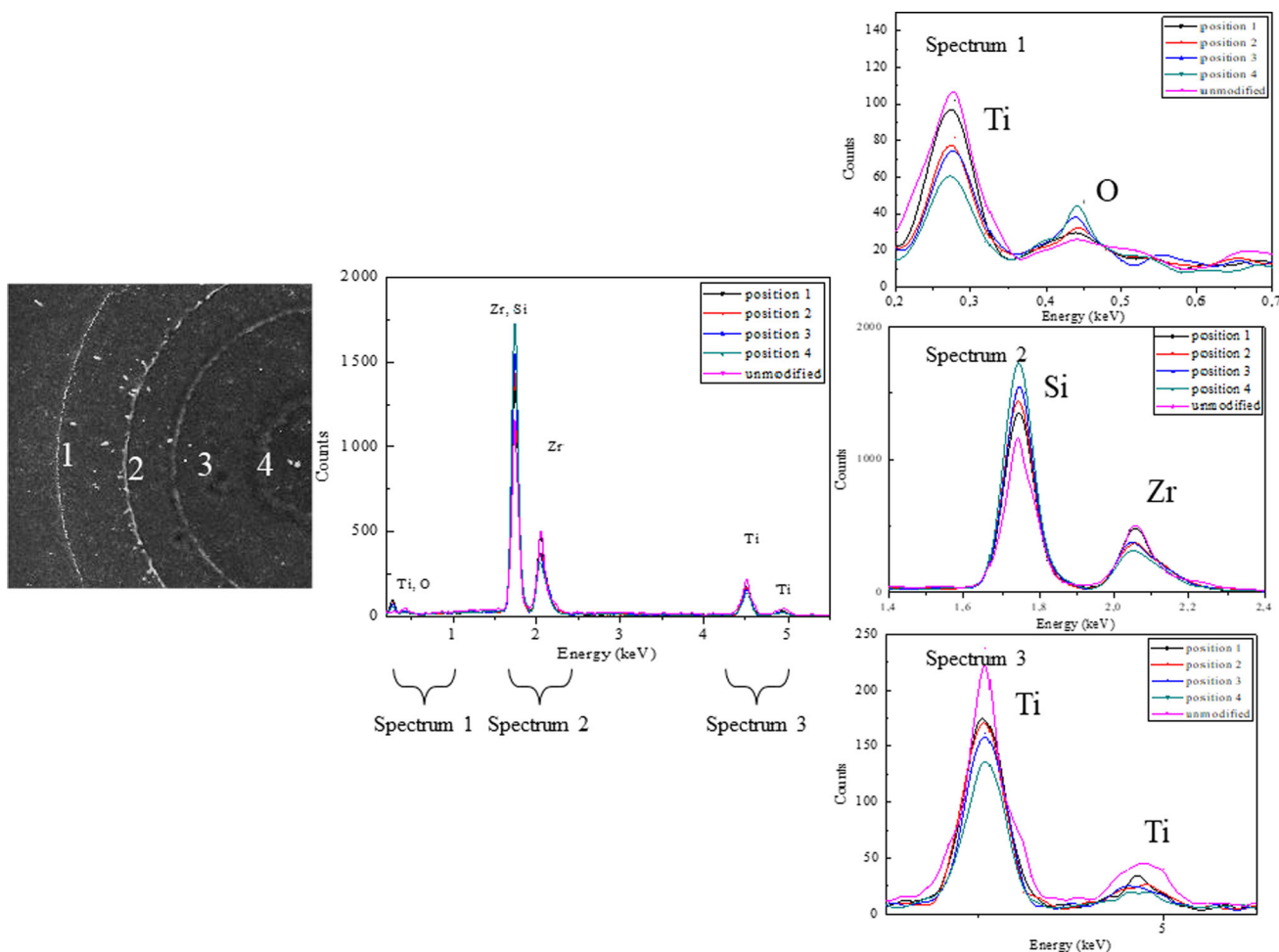


Fig. 3 EDS spectra for the marked positions of the ablated steps at the surface of the multilayer 15x(Ti/Zr) /Si system in the spot made by fs modification at 17 μJ average pulse energy

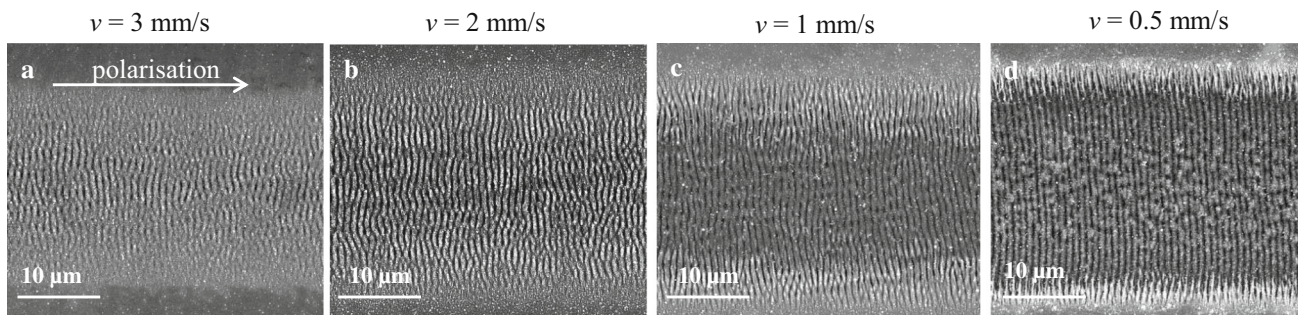


Fig. 4 SEM images for the created lines during the fs modification at the pulse energy of 2.5 μJ with different scan velocities: **a** 3 mm s⁻¹, **b** 2 mm s⁻¹, **c** 1 mm s⁻¹ and **d** 0.5 mm s⁻¹

sive ablation of the multilayer 15x(Ti/Zr) /Si thin film. On the other hand, in the case when the scan was performed parallel to the polarization direction, the periodicity has a value higher approximately 100–130 nm compared to the orthogonal scan in the polarization direction (Fig. 6). Based on this experimental observation, it can be established that the spatial periodicity of the formed LIPSS (LSFL) is quite sensitive to changes in laser parameters (the effective number of

pulses and laser polarization), as well as the nature of the material. The spatial periods varied in a wide range, which depended on the number of generated carriers in the conduction band of the laser excited materials, and the applied laser pulses [32]. The density of generated carriers for excited multilayer 15x(Ti/Zr)/Si thin film increases with increasing number of pulses, consequently the ripples with lower periods occurred.

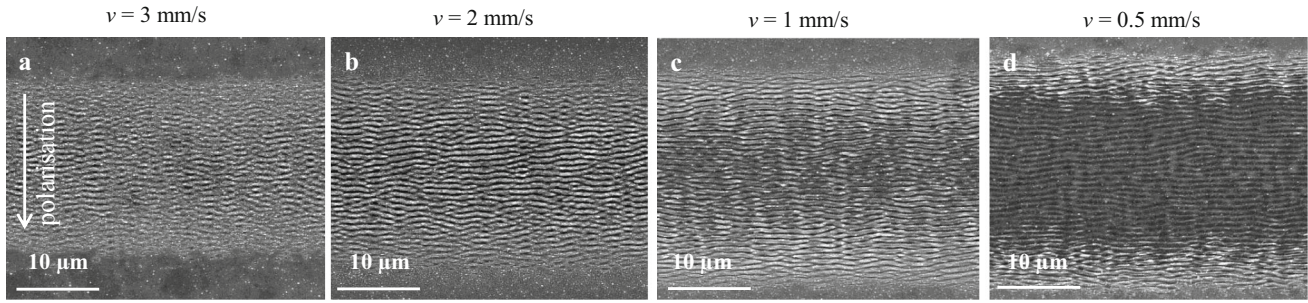


Fig. 5 SEM images for the created lines during the fs modification at the pulse energy of 2.5 μ J with changed laser polarisation for 90° at the different scan velocities: **a** 3 mm s⁻¹, **b** 2 mm s⁻¹, **c** 1 mm s⁻¹ and **d** 0.5 mm s⁻¹

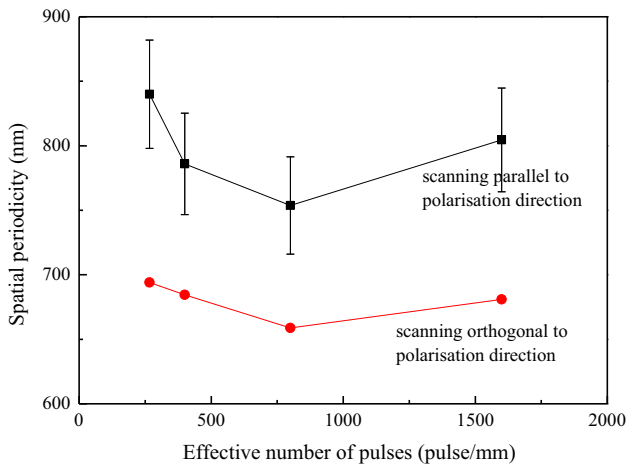


Fig. 6 Spatial periodicities of LIPSS in function of effective number of pulses, after fs modification with different laser polarisation

4 Theoretical model-simulation procedure

To interpret the experimental observations, simulations have been conducted to explore the thermal response of the multiple layered structure 15x(Ti/Zr) after irradiation with single laser pulses of pulse duration $\tau_p = 160$ fs and wavelength $\lambda_L = 1030$ nm. It is also noted that the multilayered structure is placed on a silicon substrate (in which $T_L^{(Si)}$ corresponds to its lattice temperature). Due to the fact that the laser spot radius is substantially larger than the film thickness, an 1D-Two Temperature Model (TTM) [33] can sufficiently describe the [34] relaxation process following electron excitation due to laser heating through the following equations:

$$\begin{aligned}
 C_e^{(i)} \frac{\partial T_e^{(i)}}{\partial t} &= \frac{\partial}{\partial z} \left(k_e^{(i)} \frac{\partial T_e^{(i)}}{\partial z} \right) - G_{eL}^{(i)} (T_e^{(i)} - T_L^{(i)}) \\
 &+ S^{(i)}(z, t) \quad [S^{(i)} = 0, \text{ for } i > 1] \\
 C_L^{(i)} \frac{\partial T_L^{(i)}}{\partial t} &= \frac{\partial}{\partial z} \left(k_L^{(i)} \frac{\partial T_L^{(i)}}{\partial z} \right) + G_{eL}^{(i)} (T_e^{(i)} - T_L^{(i)}) \quad (1)
 \end{aligned}$$

$$\begin{aligned}
 S^{(1)}(z, t) &= \frac{\alpha(1 - R - T)\sqrt{4 \log 2 F}}{\sqrt{\pi} \tau_p} \\
 &\exp \left(-4 \log 2 \left(\frac{t - 3\tau_p}{\tau_p} \right)^2 \right) \exp(-\alpha z) \quad (2)
 \end{aligned}$$

while $C_L^{(S)} \frac{\partial T_L^{(S)}}{\partial t} = \frac{\partial}{\partial z} \left(k_L^{(S)} \frac{\partial T_L^{(S)}}{\partial z} \right)$ describes the heat diffusion in the Si substrate. In Eqs. 1–2, $T_e^{(i)}(T_L^{(i)})$ stands for the electron (lattice) temperature of layer i ($i = 1, 3, 5, \dots, 2n - 1$ for Ti layer, $i = 2, 4, 6, \dots, 2n$ for Zr layer, for $n = 15$ Ti/Zr multilayer system). The thermo-physical properties of the material such as electron and lattice heat capacity, $(C_e^{(i)}, C_L^{(i)})$, electron and lattice heat conductivity $(k_e^{(i)} \equiv k_{e0}^{(i)} \left(B^{(i)} T_L^{(i)} / \left(A^{(i)} (T_e^{(i)})^2 + B^{(i)} T_L^{(i)} \right) \right), k_L^{(i)} \sim .01 k_e^{(i)})$, electron–phonon coupling strengths $(G_{eL}^{(i)})$ and model parameters used in the simulations are listed in Table 1. For Si, $C_L^{(S)} = 10^6(1.978 + 3.54 \times 10^{-4} T_L^{(S)} - 3.68 (T_L^{(S)})^{-2})$ [Jm⁻³K⁻¹] and $k_L^{(S)} = 158500 (T_L^{(S)})^{-1.23}$ [Jm⁻¹s⁻¹K⁻¹] [17]. Equations 1, 2 are solved by using an iterative Crank–Nicolson scheme based on a finite-difference method. For initial conditions, we choose thermal equilibrium at $T_e(z, t = 0) = T_L(z, t = 0) = 300$ K. Adiabatic boundary conditions are considered on the surface (at $z = 0, k_e^{(Ti)} \frac{\partial T_e^{(Ti)}}{\partial z} = k_L^{(Ti)} \frac{\partial T_L^{(Ti)}}{\partial z} = 0$). Furthermore, at the interface between two layers, the following conditions are applied: $T_L^{(Ti)} = T_L^{(Zr)}$, $T_e^{(Ti)} = T_e^{(Zr)}$, $k_L^{(Ti)} \frac{\partial T_L^{(Ti)}}{\partial z} = k_L^{(Zr)} \frac{\partial T_L^{(Zr)}}{\partial z}$, $k_e^{(Ti)} \frac{\partial T_e^{(Ti)}}{\partial z} = k_e^{(Zr)} \frac{\partial T_e^{(Zr)}}{\partial z}$ while on the interface between the last layer (Zr) and the substrate (Si), the following boundary conditions are used: $T_L^{(Si)} = T_L^{(Zr)}$ and $k_L^{(Si)} \frac{\partial T_L^{(Si)}}{\partial z} = k_L^{(Zr)} \frac{\partial T_L^{(Zr)}}{\partial z}$. We note that in the above formulation, for the sake of simplicity, the inclusion of latent heat for evaporation or melting has been neglected [17, 35].

While Eq. 2 provides the general expression of the form of the source term due to material heating with a pulsed laser that includes the absorption coefficient α , the reflectivity R and the transmission coefficient T of the material, the Transfer Matrix Method [34] is used

Table 1 Simulation parameters chosen for Ti and Zr

Parameter	Ti	Zr
G_{eL} ($\text{Wm}^{-3}\text{K}^{-1}$)	Fitting [36,37]	Fitting [38]
C_e ($\text{Jm}^{-3}\text{K}^{-1}$)	Fitting [36,37]	$2.78 T_e^{(\text{Zr})}$ [39]
C_L ($\text{Jm}^{-3}\text{K}^{-1}$)	2.3521×10^6 [40]	1.6952×10^6 [40]
k_{e0} ($\text{Jm}^{-1}\text{s}^{-1}\text{K}^{-1}$)	21.9 [40]	22.6 [40]
T_{melting} (K)	1941 [40]	2128 [40]
T_{boiling} (K)	3560 [40]	4650 [40]
T_{critical} (K)	15500 [41]	8650 [41]
A ($\text{s}^{-1}\text{K}^{-2}$)	Fitting [36,37]	3.41×10^5 [38]
B ($\text{s}^{-1}\text{K}^{-1}$)	Fitting [36,37]	5.16×10^{12} [38]

to compute the optical properties of the top layer (Ti) after irradiation with pulsed laser of 1030 nm by taking into account the presence of the rest of the thin layers. Calculations yield $\alpha = 4.89 \times 10^5 \text{cm}^{-1}$ [42], $T \cong 0$, $R = 0.43$, that indicate that $\sim 57\%$ of the energy will be absorbed in the first layer, while the transmitted part of the laser energy into the second layer (Zr) is very small and it is not sufficiently high to excite the electrons in the rest of the layers (especially the second layer) and produce meaningful results. This argument justifies the use of a source term to describe laser heating only of the first layer and it is assumed that laser energy is not transmitted into the next layers.

The evaluation of the thermal response of the material following irradiation with single pulses is performed through the correlation of the simulation results with the measured ablation. As noted in previous reports, ablation may be associated to the lattice temperature exceeding the condition ($\sim 0.90T_{\text{critical}}$, where T_{critical} is the critical point temperature [17,35,43] which is the temperature at which boundaries for gas and liquid phase vanish). Another criterion also usually

employed is the boiling temperature of the material, T_{boiling} , (i.e. the region of the material that is characterised with lattice temperatures higher than T_{boiling} is removed [44]). Finally, non-thermal mechanical stress-related processes (i.e. spallation) have also been used to describe ablation [45,46]. Our simulations and comparison with experimental observations indicate that the first layer (Ti) is totally removed at fluence $F = 220 \text{mJcm}^{-2}$. This value corresponds to fluence that is sufficient to raise the temperature of the upper layer above T_{boiling} ; therefore, the boiling temperature is regarded as a reliable ablation threshold criterion. Theoretical calculations of the lattice temperatures based on the scheme described above yield a spatio-temporal evolution that is illustrated in (Fig. 7a, b). The jump of lattice temperatures at the interfaces is related to the differences in the thermophysical properties of the materials (i.e. heat conductivities, heat capacities) and the electron-phonon coupling constants. It is noted that only the first three Ti/Zr layers thermally respond to the heat transfer (Fig. 7a). It is noted that to take into account ablation, all lattice points with temperatures higher than the boiling point are removed and they do not continue to heat up.

It is important to note that due to the fact that lattice temperatures on the second layer (Zr) are lower than the boiling temperature for Ti, no material is predicted to be removed from the second layer. On the other hand, it is evident that the lattice temperature attained from a large part of the second layer (Zr) for $F = 220 \text{mJcm}^{-2}$ is above the melting point of the material (2128 K). This indicates that fluid dynamics and re-solidification processes are expected to modify further the surface profile of the assembly. Therefore, appropriate phase changes-related corrections need to be incorporated into the model for a more accurate description of the surface modifica-

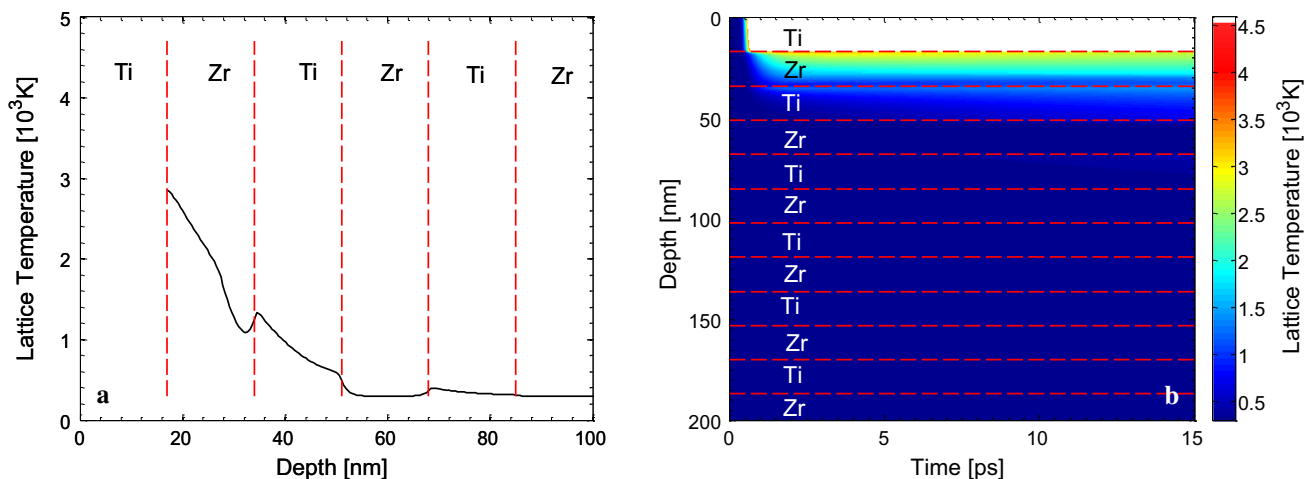


Fig. 7 **a** Spatial lattice temperature profile at $t = 15$ ps, vertical dashed lines indicate the border of each layer. **b** Lattice temperature field evolution in depth, perpendicular to the surface of the sample (white region indicates material removal; horizontal dashed lines indicate the borders of each layer). ($F = 220 \text{mJcm}^{-2}$, $\tau_p = 160$ fs, laser beam wavelength is 1030 nm). Only six (three) of the fifteen Ti/Zr layers for the lattice temperature field (spatial temperature distribution across the depth) are presented as thermal response at greater depths is minimal

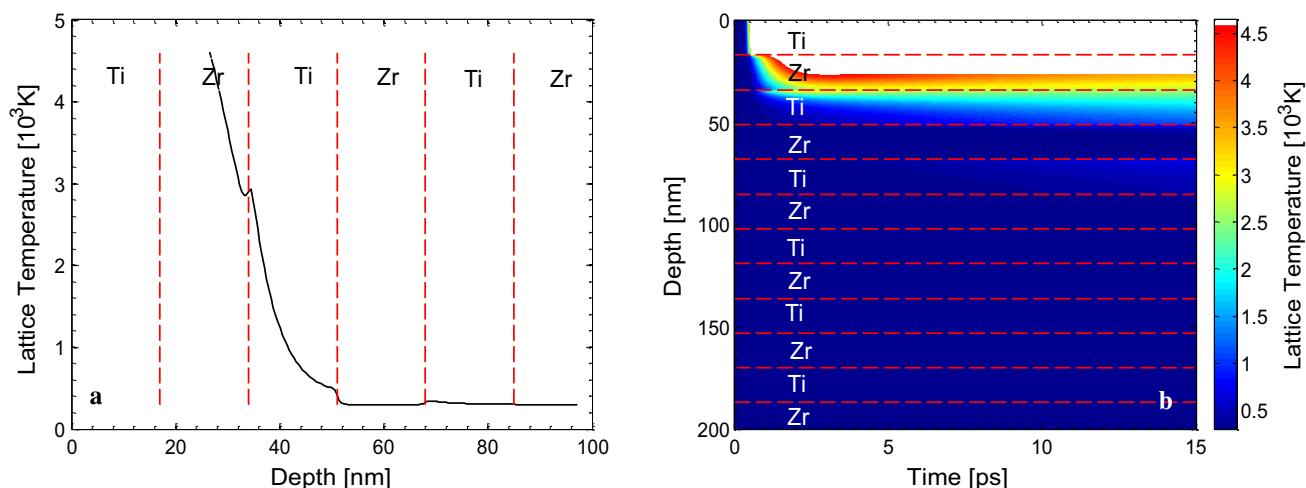


Fig. 8 **a** Spatial lattice temperature profile at $t = 3$ ps, vertical dashed lines indicate the border of each layer). **b** Lattice temperature field evolution in depth, perpendicular to the surface of the sample (white region indicates material removal; horizontal dashed lines indicate the borders of each layer). ($F = 600 \text{ mJ cm}^{-2}$, $\tau_p = 160$ fs, Laser beam wavelength is 1030 nm). Only six (three) of the fifteen Ti/Zr layers for the lattice temperature field (spatial temperature distribution across the depth) are presented as thermal response at greater depths is minimal

tion processes and determination of the morphological changes. A thorough approach requires the inclusion of Navier–Stokes equations (to describe fluid dynamics) and relevant equations to account for evaporation [17, 47–49]. Furthermore, in order to describe effects due to scanning an appropriate modification to the model and the intensity profile should be incorporated [50]. Certainly, a more rigorous description of the thermalization processes, a microscopic analysis of nonequilibrium phase-transition mechanisms through the use of hybrid molecular-dynamics-TTM models [51] should be considered towards providing a complete picture of the ultrafast processes.

Nevertheless, as the predominant objective of the work is to demonstrate that the laser energy used in the experiment is sufficient to remove the upper layer, simulations are performed, to first approximation, by ignoring hydrodynamics-generated effects.

The thermal response of the irradiated material is also explored for a higher value of fluence, $F = 600 \text{ mJ cm}^{-2}$ to evaluate structural effects on the second layer (Zr). Simulation results demonstrate that apart from the upper Ti layer that is removed, a small portion of the second layer (Zr) of thickness equal to 10 nm is also ablated as the attained temperature exceeds the boiling point (Fig. 8).

5 Conclusion

The static and dynamic femtosecond laser ablation of the multilayer 15x(Ti/Zr)/Si system were experimental and theoretical analysed based on morphological and composition changes. Selective layer-by-layer ablation was recorded during the static femtosecond irradiation, applying pulse energy in range of 10–17 μJ . The circu-

lar ablated spot with a distinct sharp boundary between unmodified and ablated areas occurred in the form of shallow and flat crater. The tendency of increasing the number of ablated concentric circles continues up to pulse energies of 15 μJ and 17 μJ , whereby for sufficiently high pulse energies the circles disappeared. In the theoretical simulation of the static fs modification, it is established that the maximum achieved temperature in the first top Ti layer was comparable to T_{boiling} and the experimental observation that the Ti layer is completely removed was confirmed at the fluence of ablation threshold.

The dynamic femtosecond irradiation of multilayer 15x(Ti/Zr)/Si structure is considered during the formation of lines with different scan velocities at the constant pulse energy (2.5 μJ) and with both laser beam polarisation (parallel and normal to scan direction). For the selected scan velocities range (0.5–3 mm s^{-1}), in all cases, the creation of the laser-induced periodic surface structure (LIPSS) was recorded, but with different spatial periodicity. The reduction in the LIPSS periodicity was continued up to 800 pulses, when the periodicities in both cases are increased due to the LIPSS generation on Si substrate.

The selective layer-by-layer ablation at static fs modification and LIPSS forming conditioned by the dynamic fs irradiation regime may provide an additional direction for controlling and optimizing of the laser texturing of the complex systems.

Acknowledgements This project has received funding from the EU-H2020 research and innovation programme under grant agreement N 654360 having benefitted from the access provided by Foundation for Research and Technology Hellas (FORTH) access provider (Institute of Electronic Structure and Lasers i.e. Institution) in Heraklion,

Crete, Greece within the framework of the NFFA-Europe Transnational Access Activity. The research was funded by the Ministry of Education, Science and Technological Development of the Republic of Serbia. Support from COST Action CA17126 - TUMIEE (supported by COST-European Cooperation in Science and Technology) is also acknowledged.

Data Availability Statement This manuscript has no associated data or the data will not be deposited. [Authors' comment: All results and data are presented in this manuscript.]

Open Access This article is licensed under a Creative Commons Attribution 4.0 International License, which permits use, sharing, adaptation, distribution and reproduction in any medium or format, as long as you give appropriate credit to the original author(s) and the source, provide a link to the Creative Commons licence, and indicate if changes were made. The images or other third party material in this article are included in the article's Creative Commons licence, unless indicated otherwise in a credit line to the material. If material is not included in the article's Creative Commons licence and your intended use is not permitted by statutory regulation or exceeds the permitted use, you will need to obtain permission directly from the copyright holder. To view a copy of this licence, visit <http://creativecommons.org/licenses/by/4.0/>.

References

1. J. Meijer, Laser beam machining (LBM), state of the art and new opportunities. *J. Mater. Process. Technol.* **149**, 2–17 (2004)
2. S. Nolte, F. Schrepel, F. Dausinger, *Ultrashort Pulse Laser Technology—Laser Sources and Applications* (Springer, Cham, 2015)
3. E. Stratakis, Nanomaterials by ultrafast laser processing of surfaces. *Sci. Adv. Mater.* **4**, 407–431 (2012)
4. L.L. Sartinska, S. Barchikovski, N. Wagenda, B.M. Rud, I.I. Timofeeva, Laser induced modification of surface structures. *Appl. Surf. Sci.* **253**, 4295–4299 (2007)
5. K. Sugioka, Progress in ultrafast laser processing and future prospects. *Nanophotonics* **6**(2), 393–413 (2017)
6. A.Y. Vorobyev, C. Guo, Direct femtosecond laser surface nano/microstructuring and its applications. *Laser Photon. Rev.* **7**, 385–407 (2013)
7. V. Zorba, L. Persano, D. Pisignano, A. Athanassiou, E. Stratakis, R. Cingolani, P. Tzanetakis, C. Fotakis, Making silicon hydrophobic: wettability control by two length scale simultaneous patterning with femtosecond laser irradiation. *Nanotechnology* **17**, 3234 (2006)
8. V. Villerius, H. Kooiker, J. Posta, Y.T. Pei, Ultrashort pulsed laser ablation of stainless steels. *Int. J. Mach. Tool Manuf.* **138**, 27–35 (2019)
9. Y.N. Kulchin, O.B. Vitrik, A.A. Kuchmizhak, V.I. Emelyanov, A.A. Ionin, S.I. Kudryashov, S.V. Makarov, Formation of crownlike and related nanostructures on thin supported gold films irradiated by single diffraction-limited nanosecond laser pulses. *Phys. Rev. E* **90**, 0230171–0230177 (2014)
10. B.S. Yilbas, A.F.M. Arif, C. Karatas, K. Raza, Laser treatment of aluminium surface: analysis of thermal stress field in the irradiated region. *J. Mater. Process. Technol.* **209**, 77–88 (2009)
11. Y. Hwang, A.Y. Vorobyev, C. Guo, Surface-plasmon-enhanced photoelectron emission from nanostructure-covered periodic grooves on metals. *Phys. Rev. B* **79**, 0854251–0854254 (2009)
12. R. Le Harzic, N. Huot, E. Audouard, C. Jonin, P. Laporte, Comparison of heat-affected zones due to nanosecond and femtosecond laser pulses using transmission electronic microscopy. *Appl. Phys. Lett.* **80**, 3886–3888 (2002)
13. C. Momma, B.N. Chichkov, S. Nolte, F. von Alvensleben, A. Tunnermann, H. Welling, B. Wellegehausen, Short-pulse laser ablation of solid targets. *Opt. Commun.* **129**, 134–142 (1996)
14. J. Kruger, W. Kautek, Femtosecond-pulse visible laser processing of transparent materials. *Appl. Surf. Sci.* **96–98**, 430–438 (1996)
15. I.N. Saraeva, S.I. Kudryashov, V.N. Lednev, S.V. Makarov, S.M. Pershin, A.A. Rudenko, D.A. Zayarny, A.A. Ionin, Single- and multishot femtosecond laser ablation of silicon and silver in air and liquid environments: plume dynamics and surface modification. *Appl. Surf. Sci.* **476**, 576–586 (2019)
16. S. Petrović, B. Gaković, E. Peruško, I. Bogdanović-Radović, M. Čekada, B. Jelenković, Femtosecond laser-induced periodic surface structure on the Ti-based nanolayered thin films. *J. Appl. Phys.* **114**(5), 233108 (2013)
17. G.D. Tsibidis, M. Barberoglou, P.A. Loukakos, E. Stratakis, C. Fotakis, Dynamics of ripple formation on silicon surfaces by ultrashort laser pulses in subablation conditions. *Phys. Rev. B* **86**, 115316 (2012)
18. J. Bonse, A. Rosenfeld, J. Kruger, On the role of surface plasmon polaritons in the formation of laser-induced periodic surface structures upon irradiation of silicon by femtosecond-laser pulses. *J. Appl. Phys.* **106**, 104910 (2009)
19. S. Kozyukhina, P. Lazarenko, Y. Vorobyov, A. Baranchikov, V. Glukhenkaya, M. Smayev, A. Sherchenkov, Y. Sybina, A. Polohin, V. Sigaev, Laser-induced modification and formation of periodic surface structures (ripples) of amorphous GST225 phase change materials. *Opt. Laser Technol.* **113**, 87–94 (2019)
20. A.G. Kovačević, S. Petrović, B. Bokić, B. Gaković, M.T. Bokorov, B. Vasić, R. Gajić, M. Trtica, B.M. Jelenković, Surface nano-patterning of Al/Ti multilayer thin films and Al single layer by a low-fluence UV femtosecond laser beam. *Appl. Surf. Sci.* **326**, 91–98 (2015)
21. S. Mahdis, C. Youngjae, An overview of thin film nitinol endovascular devices. *Acta Biomater.* **21**, 20–34 (2015)
22. D. Peruško, M. Mitrić, V. Milinović, S. Petrović, M. Milosavljević, The effects of pre-implantation of steel substrates on the structural properties of TiN coatings. *J. Mater. Sci.* **43**(8), 2625–2630 (2008)
23. G. Han, S. Zhang, P.P. Boix, L.H. Wong, L. Sun, S.Y. Lien, Towards high efficiency thin film solar cells. *Progr. Mater. Sci.* **87**, 246–291 (2017)
24. J. de Damborenea, Surface modification of metals by high power lasers. *Surf. Coat. Technol.* **100**(101), 377–82 (1998)

25. S. Petrović, D. Peruško, E. Skoulas, J. Kovač, M. Mitrić, J. Potočnik, Z. Rakočević, E. Stratakis, Laser-assisted surface texturing of Ti/Zr multilayers for mesenchymal stem cell response. *Coatings* **9**, 854–866 (2019)
26. J.M. Liu, Simple technique for measurements of pulsed Gaussian-beam spot sizes. *Opt. Lett.* **7**, 196–198 (1982)
27. P.T. Mannion, J. Magee, E. Coyne, G.M. O'Connor, T.J. Glynn, The effect of damage accumulation behaviour on ablation thresholds and damage morphology in ultrafast laser micro-machining of common metals in air. *Appl. Surf. Sci.* **233**, 275–287 (2004)
28. B. Liu, W. Wang, G. Jiang, X. Mei, K. Wang, J. Wang, Formation of porous structure with subspot size under the irradiation of picosecond laser pulses. *J. Nanomater.* **2013**, 301301 (2013)
29. S. Petrović, D. Peruško, J. Kovač, Z. Siketić, I. Radović-Bogdanović, B. Gaković, B. Radak, M. Trtica, Laser-induced surface oxidation of (Ni/Ti)/Si system with picosecond laser pulses. *Mater. Chem. Phys.* **143**, 530–535 (2014)
30. J. Bonse, R. Koter, M. Hartelt, D. Spaltmann, S. Pentzien, S. Höhm, A. Rosenfeld, J. Krüger, Tribological performance of femtosecond laser-induced periodic surface structures on titanium and a high toughness bearing steel. *Appl. Surf. Sci.* **336**, 21–27 (2015)
31. I. Gnilytskyi, T.J.-Y. Derrien, Y. Levy, N.M. Bulgakova, T. Mocek, L. Orazi, High-speed manufacturing of highly regular femtosecond laser-induced periodic surface structures: physical origin of regularity. *Sci. Rep.* (2017). <https://doi.org/10.1038/s41598-017-08788-z>
32. J. Bonse, J. Kruger, Pulse number dependence of laser-induced periodic surface structures for femtosecond laser irradiation of silicon. *J. Appl. Phys.* **108**(5), 034903 (2010)
33. B. Gaković et al., Partial ablation of Ti/Al nano-layer thin film by single femtosecond laser pulse. *J. Appl. Phys.* **122**(22), 223106 (2017)
34. M. Born, E. Wolf, *Principles of Optics: Electromagnetic Theory of Propagation, Interference and Diffraction of Light*, 7th edn. (Cambridge University Press, Cambridge, 1999)
35. R. Kelly, A. Miotello, Comments on explosive mechanisms of laser sputtering. *Appl. Surf. Sci.* **96–98**, 205–215 (1996)
36. G.D. Tsibidis, Thermal response of double-layered metal films after ultrashort pulsed laser irradiation: The role of nonthermal electron dynamics. *Appl. Phys. Lett.* **104**(5), 051603 (2014)
37. Z. Lin, L.V. Zhigilei, V. Celli, Electron-phonon coupling and electron heat capacity of metals under conditions of strong electron-phonon nonequilibrium. *Phys. Rev. B* **77**(7), 075133 (2008)
38. S. Marinier, L.J. Lewis, Femtosecond laser ablation of CuxZr1-x bulk metallic glasses: a molecular dynamics study. *Phys. Rev. B* (2015). <https://doi.org/10.1103/PhysRevB.92.184108>
39. O. Jepsen, O.K. Andersen, A.R. Mackintosh, Electronic structure of hcp transition-metals. *Phys. Rev. B* **12**(8), 3084–3103 (1975)
40. D.R. Lide, *CRC Handbook of Chemistry and Physics*, 84th edn. (CRC Press, Boca Raton, 2003-2004)
41. A.L. Horvath, Critical temperature of elements and the periodic system. *J. Chem. Educ.* **50**(5), 335 (1973)
42. P.B. Johnson, R.W. Christy, Optical constants of transition metals: Ti, V, Cr, Mn, Fe Co, Ni, and Pd. *Phys. Rev. B* **9**(12), 5056–5070 (1974)
43. J.K. Chen, J.E. Beraun, Modelling of ultrashort laser ablation of gold films in vacuum. *J. Opt. A-Pure Appl. Opt.* **5**(3), 168–173 (2003)
44. G.D. Tsibidis et al., Modelling periodic structure formation on 100Cr6 steel after irradiation with femtosecond-pulsed laser beams. *Appl. Phys. A* **124**(1), 27 (2017)
45. E. Leveugle, D.S. Ivanov, L.V. Zhigilei, Photomechanical spallation of molecular and metal targets: molecular dynamics study. *Appl. Phys. A* **79**(7), 1643–1655 (2004)
46. C. Wu, L.V. Zhigilei, Microscopic mechanisms of laser spallation and ablation of metal targets from large-scale molecular dynamics simulations. *Appl. Phys. A* **114**(1), 11–32 (2014)
47. G.D. Tsibidis et al., Convection roll-driven generation of supra-wavelength periodic surface structures on dielectrics upon irradiation with femtosecond pulsed lasers. *Phys. Rev. B* **94**(8), 081305(R) (2016)
48. G.D. Tsibidis, C. Fotakis, E. Stratakis, From ripples to spikes: a hydrodynamical mechanism to interpret femtosecond laser-induced self-assembled structures. *Phys. Rev. B* **92**(4), 041405(R) (2015)
49. A. Papadopoulos et al., Formation of periodic surface structures on dielectrics after irradiation with laser beams of spatially variant polarisation: a comparative study. *Appl. Phys. A* **124**(2), 146 (2018)
50. E. Allahyari, J.J.J. Nivas, E. Skoulas, R. Bruzzese, G.D. Tsibidis, E. Stratakis, S. Amoroso, On the formation and features of the supra-wavelength grooves generated during femtosecond laser surface structuring of silicon. *Appl. Surf. Sci.* **528**, 146607 (2020)
51. D.S. Ivanov, L.V. Zhigilei, Combined atomistic-continuum modeling of short-pulse laser melting and disintegration of metal films. *Phys. Rev. B* **68**, 064114 (2003)